Large-gap quantum anomalous Hall effect in monolayer halide perovskite

Zeyu Li,[1] Yulei Han ⦿,[2,1] and Zhenhua Qiao ⦿[1,*]

[1]*ICQD, Hefei National Laboratory for Physical Sciences at Microscale, CAS Key Laboratory of Strongly-Coupled Quantum Matter Physics, and Department of Physics, University of Science and Technology of China, Hefei, Anhui 230026, China*
[2]*Department of Physics, Fuzhou University, Fuzhou, Fujian 350108, China*

We theoretically propose a family of structurally stable monolayer halide perovskite $A_3B_2C_9$ (A = Rb, Cs; B = Pd, Pt; C = Cl, Br) with easy magnetization planes. The family materials are all half metals with large spin gaps beyond 1 eV accompanying a single spin Dirac point located at K point. When the spin-orbit coupling is switched on, we further show that $Rb_3Pt_2Cl_9$, $Cs_3Pd_2Cl_9$, and $Cs_3Pt_2Cl_9$ monolayers can open up large band gaps from 63 to 103 meV to harbor quantum anomalous Hall effect with Chern numbers of $\mathcal{C} = \pm 1$ whenever the mirror symmetry is broken by the in-plane magnetization, and the corresponding Berezinskii-Kosterlitz-Thouless transition temperatures are over 248 K. Our findings provide a potentially realizable platform to explore quantum anomalous Hall effect and spintronic applications at high temperatures.

I. INTRODUCTION

Due to the topological protection from spatial separation, the Landau-level induced chiral edge modes make quantum Hall effect appealing in designing future low-power electronics [1]. In early time, the requirement of a strong magnetic field severely prevents the possible application of quantum Hall effect. Ever since the experimental discovery of graphene and topological insulators, various recipes were proposed to produce the quantum Hall effect without an external magnetic field, i.e., quantum anomalous Hall effect (QAHE). Two representative categories are monolayer atomic crystals (e.g., graphene and graphenelike materials) [2–4] and magnetic topological insulators [5–8]. On one side, in 2010 it was theoretically reported that graphene can open up a band gap to harbor QAHE in the presence of both Rashba spin-orbit coupling and exchange field [3]. However, although there has been tremendous progress towards approaching the quantization of anomalous Hall effect, i.e., $1/4e^2/h$, experimental realization of QAHE in graphene is still a challenge due to the weak Rashba spin-orbit coupling [9,10]. On the other side, nearly at the same time, a magnetic topological insulator was theoretically proposed to host QAHE via Cr dopants, and such a scheme was soon successfully realized in experiment at the extremely low temperature of 30 mK after three years' efforts [11]. When more attention was focused on how to enhance the QAHE observation temperature, it was experimentally reported that the antiferromagnetic $MnBi_2Te_4$ thin flakes can reach a record-breaking temperature of 6.5 K with the aid of an external magnetic field [12–15].

Nevertheless, the current achievement is still further away from the practical application. As an important material family, the perovskite ABO_3 consists of transition metal and heavy elements [16–20], implying a wonderland for breeding topological states, such as topological insulator, topological node-line semimetal, and topological crystalline metal [21–24]. Besides, several theoretical proposals have been suggested by building superlattices with a (111) bilayer rare-earth perovskite embedded inside wide-gap perovskites [25–28], where the major experimental difficulty is the requirement of precise alignment at the interfaces. Inspired by the broad interest of two-dimensional materials, the two-dimensional layered perovskites have also been experimentally prepared, e.g., 111-type In-based halide perovskite $Cs_3In_2Cl_9$ [29,30]. The layered perovskite materials display the possibility of realizing the QAHE due to their large intrinsic spin-orbit coupling and magnetism.

In this work, we theoretically predict a two-dimensional halide perovskite material family $A_3B_2C_9$, where A, B, and C represent alkali metal element (Rb, Cs), transition metal element (Pd, Pt), and halogen element (Cl, Br), respectively. They share the same structure as the monolayer $Cs_3In_2Cl_9$ with the transition metal atoms forming a buckled honeycomb lattice linked by halogen atoms. By performing first-principles calculations, we find that they are all half metals, with a huge spin splitting over 1.0 eV. The single spin Dirac point emerging at the K point is topologically protected by the trigonal crystal symmetry [31–33]. After the spin-orbit coupling is switched on, topologically nontrivial band gaps hosting QAHE open in monolayers $Rb_3Pt_2Cl_9$, $Cs_3Pt_2Cl_9$, and $Cs_3Pd_2Cl_9$, when the vertical mirror symmetry is broken by the magnetization. For the magnetization lying inside the plane, the nontrivial gaps can reach up to 103, 69, and 93 meV at the HSE06 level, greatly exceeding room temperature. Tuning the magnetization direction from in plane to out of plane will raise the gaps to 137, 99, and 100 meV, respectively. Monte Carlo calculations show that these three materials own a high Berezinskii-Kosterlitz-Thouless transition temperature above 248 K, implying the quasi-long-range order can be

*Correspondence author: qiao@ustc.edu.cn

observed at high temperatures like $CoPS_3$ [34]. The successful synthesis of $Cs_3Fe_2Cl_9$ [35] strongly indicates the possibility of realizing high temperature QAHE in our proposed monolayer halide perovskites.

II. CALCULATION METHODS

Our calculations were performed using the projected-augmented-wave method as implemented in the VASP package [36], and the generalized gradient approximation exchange-correlation [37] potential was used. The kinetic cutoff energy of the plane wave was set to be 500 eV. The Brillouin zone was sampled with a Γ-centered $13 \times 13 \times 1$ grid based on the scheme proposed by Monkhorst and Pack for calculation of structural optimization and magnetic property, whereas a $6 \times 6 \times 1$ grid was used for electronic structures [38]. A vacuum buffer space over 20 Å was included to prevent interaction between adjacent slabs. The convergence criterion was set to be 10^{-8} eV and 10^{-7} eV for energy in optimization and self-consistent field calculations, respectively. During structural optimization, all atoms were fully relaxed, and forces were converged to less than 0.0005 eV/Å. The phonon calculations were carried out by using the density functional perturbation theory as implemented in the PHONOPY package with a $2 \times 2 \times 1$ supercell [39]. The screened hybrid functional (HSE06) method was applied to predict band gap closing to experiments [40]. The maximally localized Wannier functions were constructed by using the software package WANNIER90 with interfacing VASP [41,42]. The anomalous Hall conductivity was obtained by the interpolation of maximally localized Wannier functions. The anomalous Hall conductivity was obtained by summing Berry curvatures over all occupied valence bands:

$$\sigma_{\alpha\beta} = -\frac{e^2}{\hbar} \int_{BZ} \frac{dk}{(2\pi)^2} \sum_n f_n(k)\Omega_{n,\alpha\beta}(k). \qquad (1)$$

The edge state was calculated by the iterative Green's function method as implemented in the WANNIERTOOLS package [43]. Mcsolver code was used to perform Monte Carlo simulations on a 30×30 supercell with 200 000 steps at each temperature [44].

III. STRUCTURAL AND MAGNETIC PROPERTIES

Monolayer $A_3B_2C_9$ is crystallized in P-$3m1$ space group (No. 164), as depicted in Fig. 1(a). There are three vertical mirror planes across the high symmetry M point in the corresponding first Brillouin zone as shown in Fig. 1(b). Its primitive cell contains three alkaline metal atoms, two transition metal atoms, and nine halogen atoms. Each transition metal atom is surrounded by six nearest halogen atoms forming distorted octahedra. Monolayer $A_3B_2C_9$ exhibits five atomic layers, with transition metal atoms being located at different layers to form a buckled honeycomb lattice in favor of acquiring the Dirac point in electronic structure. The interaction between two transition metal atoms is bridged by a halogen atom forming the superexchange mechanism. Similar structure can be found in (111) bilayer transition metal oxide perovskite [27]. The alkali metal and halogen atoms at the outermost layers form a shield to protect the inner buckled
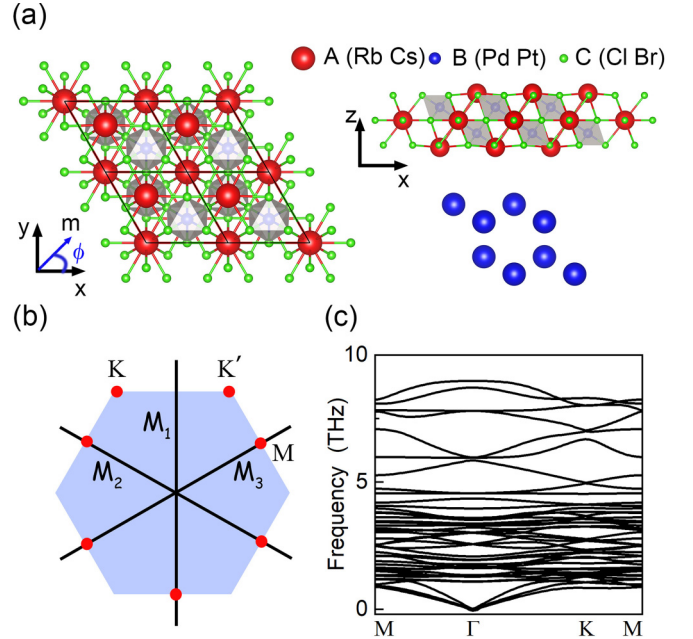

FIG. 1. (a) Top view and side view of monolayer $A_3B_2C_9$, with the transition metal atoms forming a buckled honeycomb lattice. (b) First Brillouin zone with high symmetry points, with the solid lines representing three vertical mirror planes. (c) Phonon spectra of $Cs_3Pt_2Cl_9$.

honeycomb lattice composed of transition metal atoms from degradation of environment in monolayer $A_3B_2C_9$, leading to high stability of the structures as experimentally synthesized halide perovskites $Cs_3In_2Cl_9$ and Cs_2PtI_6 [30,45]. The structural stability of monolayer $A_3B_2C_9$ is also confirmed by phonon spectrum calculations [see Fig. 1(c) and Fig. 6]. The optimized lattice constants of monolayer $A_3B_2C_9$ (A = Rb, Cs; B = Pd, Pt; C = Cl, Br) are listed in Table I. Along with the increase of the atomic number of component elements, the lattice constants increase monotonically, ranging from 7.036 to 7.582 Å within the x-y plane and 5.763 to 6.252 Å along the z direction.

To determine the ground states of monolayer $A_3B_2C_9$, four representative magnetic configurations, i.e., ferromagnetic (FM), Néel antiferromagnetic (NAFM), stripe AFM (SAFM), and zigzag AFM (ZAFM), as shown in Fig. 2(a),

TABLE I. Lattice constants, magnetic ground state (GS), and exchange coupling constants of monolayer $A_3B_2C_9$.

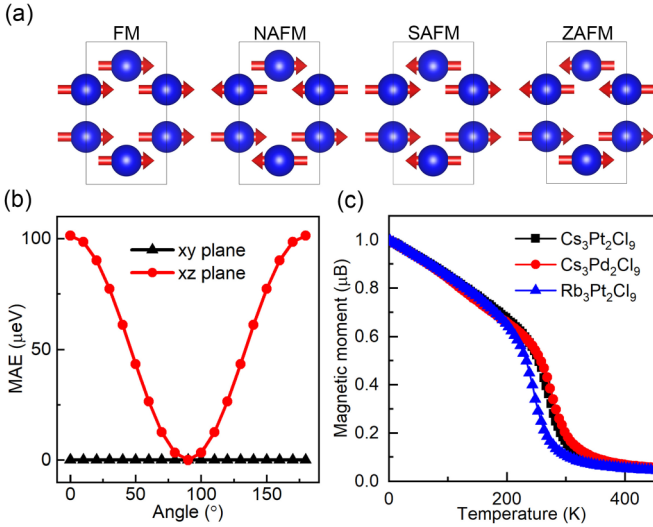|	a (Å)	c (Å)	GS	J_1 (meV)	J_2 (meV)	J_3 (meV)
$Rb_3Pd_2Cl_9$	7.036	5.763	FM	−136.0	−1.7	4.2
$Rb_3Pd_2Br_9$	7.349	5.919	FM	−9.0	−2.0	−3.0
$Rb_3Pt_2Cl_9$	7.061	5.756	FM	−123.6	−6.1	8.9
$Rb_3Pt_2Br_9$	7.385	5.898	FM	−20.5	−7.8	−3.3
$Cs_3Pd_2Cl_9$	7.215	6.091	FM	−173.3	2.3	9.1
$Cs_3Pd_2Br_9$	7.512	6.252	FM	−45.6	−4.1	−1.7
$Cs_3Pt_2Cl_9$	7.209	6.098	FM	−115.8	−20.4	23.8
$Cs_3Pt_2Br_9$	7.582	6.203	FM	−59.2	−9.9	1.1

FIG. 2. (a) Four possible magnetic configurations: FM, NAFM, SAFM, and ZAFM. (b) The magnetic anisotropic energy (MAE) of monolayer $Cs_3Pt_2Cl_9$, with red and black curves corresponding to the relative energy in x-z and x-y planes with respect to that along the x direction. (c) The normalized magnetic moment of monolayers $Rb_3Pt_2Cl_9$, $Cs_3Pt_2Cl_9$, and $Cs_3Pd_2Cl_9$ as a function of temperature by Monte Carlo simulations.

are considered. The GGA + U scheme is used to describe the on-site Coulomb repulsion on the d electrons of Pd and Pt atoms [46]. The value of U is set to be 3.5/2.5 eV for Pd/Pt, consistent with the result of the magnetic moment obtained from HSE06 calculation. The energies of different magnetic configurations are summarized in Table II, indicating that FM configuration is the most stable state for all monolayer $A_3B_2C_9$. The magnetic anisotropy energy (MAE) calculations show that the magnetization prefers to lie inside the x-y plane, such as $Cs_3Pt_2Cl_9$ shown in Fig. 2(b). The larger atomic number of occupation for each site leads to the enhanced MAE, e.g., the MAE in x-z plane increases from 62.2 μeV ($Rb_3Pd_2Cl_9$) to 2.6 meV ($Cs_3Pt_2Br_9$). Although the Mermin-Wagner theorem prohibits long-range magnetic order in two-dimensional isotropic systems, a quasi-long-range order is allowed below the Berezinskii-Kosterlitz-Thouless critical temperature, such as VS_2 and $FeCl_2$ [47–49]. Based on the XY model, the Berezinskii-Kosterlitz-Thouless transition temperature is estimated up to the third neighbor coupling

TABLE II. Total energy of per unit cell (in units of eV) for the different magnetic configurations.

$A_3B_2C_9$	FM	NAFM	SAFM	ZAFM
$Rb_3Pd_2Cl_9$	−81.162	−80.766	−80.883	−81.031
$Rb_3Pd_2Br_9$	−73.024	−72.988	−72.998	−72.998
$Rb_3Pt_2Cl_9$	−86.779	−86.435	−86.508	−86.658
$Rb_3Pt_2Br_9$	−78.297	−78.226	−78.225	−78.236
$Cs_3Pd_2Cl_9$	−81.888	−81.395	−81.551	−81.751
$Cs_3Pd_2Br_9$	−73.948	−73.806	−73.840	−73.881
$Cs_3Pt_2Cl_9$	−87.509	−87.233	−87.196	−87.383
$Cs_3Pt_2Br_9$	−79.244	−79.069	−79.086	−79.148

strength. The spin Hamiltonian is expressed as

$$H = \sum_{\langle i,j \rangle} J_1 \left(S_i^x S_j^x + S_i^y S_j^y \right) + \sum_{\langle\langle i,j \rangle\rangle} J_2 \left(S_i^x S_j^x + S_i^y S_j^y \right)$$
$$+ \sum_{\langle\langle\langle i,j \rangle\rangle\rangle} J_3 \left(S_i^x S_j^x + S_i^y S_j^y \right), \tag{2}$$

where $S^{x,y}$ is the spin operator and $\langle \ldots \rangle$, $\langle\langle \ldots \rangle\rangle$, and $\langle\langle\langle \ldots \rangle\rangle\rangle$ denote the sum over the nearest, the second, and the third neighboring sites. $J_{1,2,3}$ denote the nearest, the second, and the third neighbor exchange interaction strengths, which can be extracted from the following equations:

$$E_{\text{FM/NAFM}} = E_0 + (\pm 3J_1 + 6J_2 \pm 3J_3)|\vec{S}|^2,$$
$$E_{\text{SAFM/ZAFM}} = E_0 + (\mp J_1 - 2J_2 \pm 3J_3)|\vec{S}|^2, \tag{3}$$

where E_0 is the ground state energy and $S = 1/2$ in our system. The exchange coupling constants of monolayer $A_3B_2C_9$ are listed in Table I. The first neighbor exchange interactions are always negative and excess the second and the third neighbor exchange interactions obviously in favor of the FM state. By performing the Monte Carlo calculations, one can acquire the Berezinskii-Kosterlitz-Thouless temperature. The critical temperatures of monolayer $A_3B_2C_9$ range from 47 to 278 K [see Fig. 2(c) and Fig. 8], indicating that the quasi-long-range can be observed at relatively high temperatures as that of $CoPS_3$ [34].

IV. BAND STRUCTURES AND TOPOLOGICAL PROPERTIES

Now, let us move to the electronic properties of monolayer $A_3B_2C_9$. As depicted in Fig. 9, all $A_3B_2C_9$ monolayers are half metals with the Dirac point being located at the K point and the energy range with only one spin is over 1.0 eV, facilitating building spintronic devices with various materials. Along the high symmetry K-M line, the lowest unoccupied band crosses the Fermi level in five monolayer $A_3B_2C_9$, resulting in the absence of global gaps in the presence of spin-orbit coupling. After taking spin-orbit coupling into consideration, due to the lack of vertical mirror symmetry at K, a band gap opens regardless of the magnetization direction. Three Cl-based monolayers, i.e., $Cs_3Pd_2Cl_9$, $Cs_3Pt_2Cl_9$, and $Rb_3Pt_2Cl_9$, exhibit global band gaps. Herein below, we take the monolayer $Cs_3Pt_2Cl_9$ as an example of which the band structures are depicted in Fig. 3. In monolayer $Cs_3Pt_2Cl_9$, the Pt atom is in its +3 oxidation state with seven electrons filling the d orbitals. Because of the D_{3d}^2 space group, the distorted octahedra around the Pt atom leads to the further splitting of d orbitals as shown in Fig. 5. Six electrons fill the lower d orbitals, whereas one electron fills a half of the (d_{xz}, d_{yz}) orbital making the system half metallic with pure spin polarization at the Fermi level. Furthermore, at the high symmetric point K, the Dirac point is protected by the group of wave vectors, i.e., the D_3^2 space group which owns a two-dimensional irreducible representation leading to the robust band crossing [Fig. 3(a)]. In the appearance of spin-orbit coupling, the band crossing is gapped by a Dirac mass term. The topological properties of the gap depend on the magnetization direction, i.e., (i) when the magnetization direction, e.g., along the x
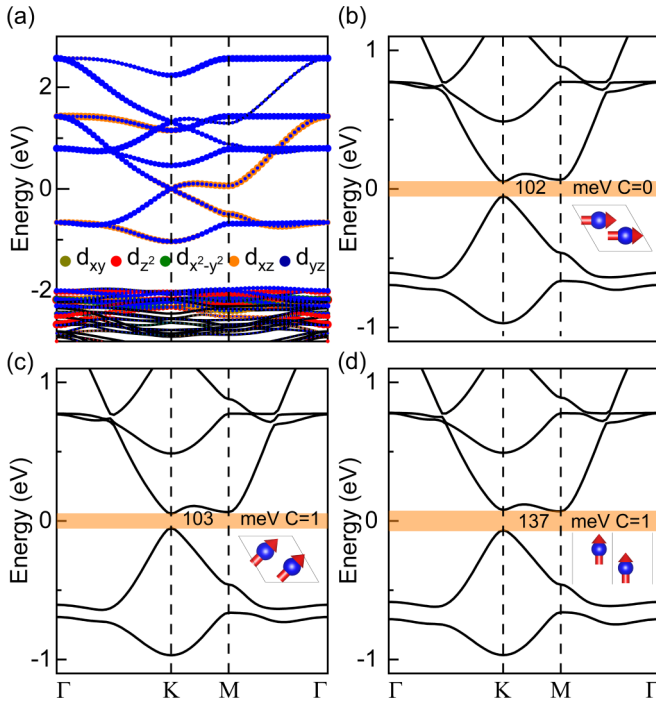
FIG. 3. (a) Orbital projected ($3d$ orbitals of Pt) band structure of monolayer $Cs_3Pt_2Cl_9$ without spin-orbit coupling where the (d_{xz}, d_{yz}) orbitals dominate the bands near the Fermi level. (b)–(d) Band structures with spin-orbit coupling when the magnetization direction is along $\phi = 0°$, $45°$ and z direction, respectively.

axis, is perpendicular to the vertical mirror plane, the band gap would be trivial due to the symmetry restriction [50,51], and (ii) the remaining magnetization direction breaks the vertical
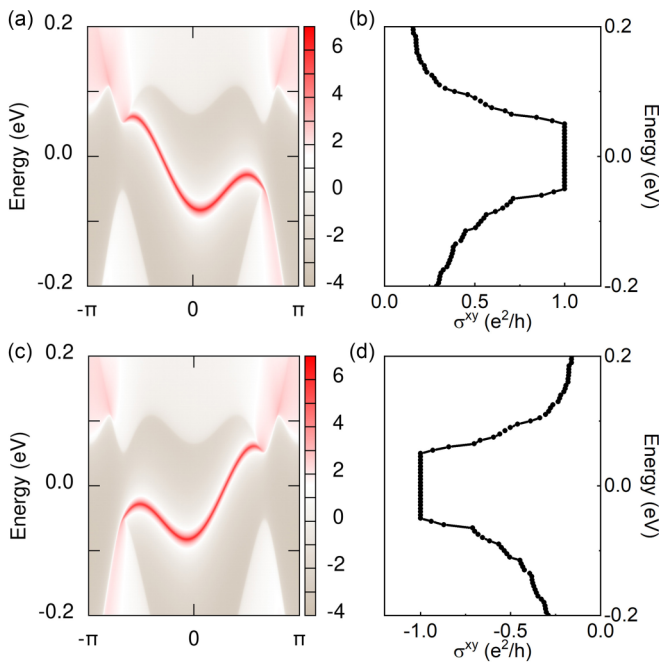
FIG. 4. Energy spectra of a semi-infinite ribbon of monolayer $Cs_3Pt_2Cl_9$ with the in-plane magnetization along $\phi = 45°$ (a) and $-45°$ (c). The corresponding anomalous Hall conductivity with $\phi = 45°$ (b) and $-45°$ (d).
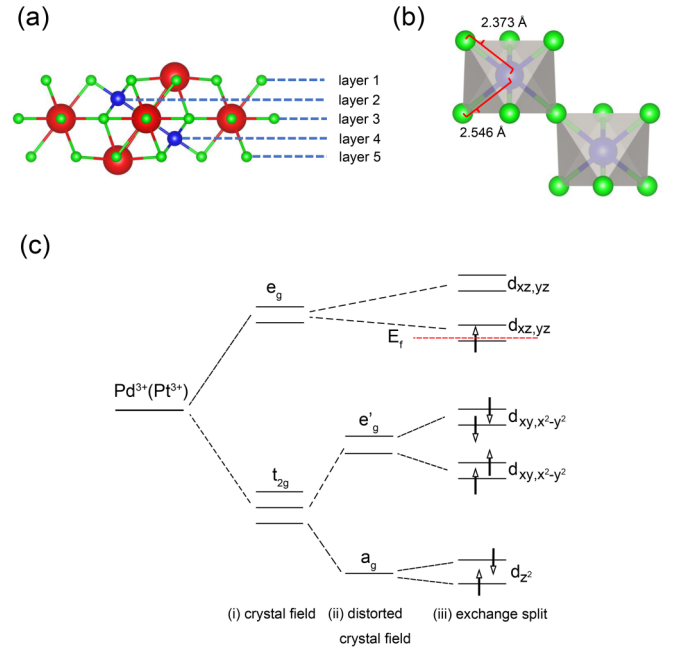
FIG. 5. (a) Five atomic layers of monolayer $A_3B_2C_9$. (b) Internal and external bond length between transition metal atom and halogen atom in monolayer $Cs_3Pt_2Cl_9$. (c) Schematic diagram of energy level splitting for d orbitals in a distorted octahedra crystal field of monolayer $A_3B_2C_9$.

mirror symmetry and induces a topologically nontrivial gap harboring QAHE. When the magnetization is along $\phi = 45°$, as displayed in Fig. 3(c), a topologically nontrivial gap with Chern number of $\mathcal{C} = 1$ can be produced. An out-of-plane magnetization further results in a larger topologically nontrivial gap up to 137 meV as shown in Fig. 3(d). Moreover, the QAHE is magnetization orientation dependent with alternating Chern numbers of $\mathcal{C} = \pm 1$ [52]. As displayed in Fig. 4, the Chern number can be tuned from $+1(-1)$ to $-1(+1)$ by rotating the magnetization direction in the x-y plane. Due to the negligible MAE in the x-y plane, a tiny magnetic field can be used to rotate the in-plane magnetization direction and enhance the effective anisotropy as employed in the $Cr_2Ge_2Te_6$ film [53], indicating the feasibility of magnetization direction tunable topological phases in our proposed systems.

V. MATERIALS SYNTHESIS

As a big materials family, halide perovskite consists of a number of two-dimensional layered materials. Except for the 111-type In-based halide perovskite $Cs_3In_2Cl_9$, it was found that $Cs_3Fe_2Cl_9$ has been synthesized in 1954 [35]. This means that through proper modulation of synthesis, it is promising to produce the materials of monolayer $A_3B_2C_9$ for the study of high temperature QAHE.

VI. SUMMARY

We theoretically proposed a two-dimensional halide perovskite family $A_3B_2C_9$ (A = Rb, Cs; B = Pd, Pt; C = Cl, Br). We find that five of them are half metals with wide fully
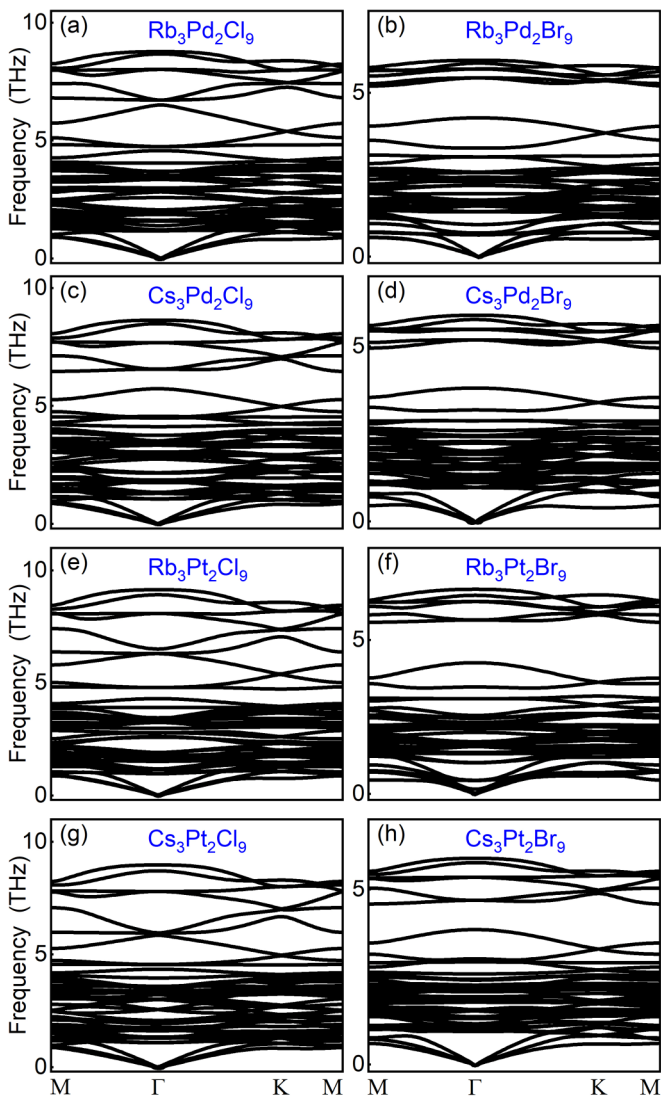
FIG. 6. (a)–(d) Phonon spectrum of monolayers (a) $Rb_3Pd_2Cl_9$, (b) $Rb_3Pd_2Br_9$, (c) $Cs_3Pd_2Cl_9$, and (d) $Cs_3Pd_2Br_9$. (e)–(h) The phonon spectrum of monolayers (e) $Rb_3Pt_2Cl_9$, (f) $Rb_3Pt_2Br_9$, (g) $Cs_3Pt_2Cl_9$, and (h) $Cs_3Pt_2Br_9$. No imaginary frequency mode emerges along the high symmetry path for all monolayers $A_3B_2C_9$.

spin-polarized energy range. When spin-orbit coupling is further considered, we show that monolayers $Cs_3Pd_2Cl_9$, $Cs_3Pt_2Cl_9$, and $Rb_3Pt_2Cl_9$ can open up topologically nontrivial band gaps of $\sim$100 meV to realize high temperature QAHE with Chern numbers of $\mathcal{C} = \pm1$. A small external magnetic field can be applied to tune the sign of Chern number by altering the magnetization direction. Our proposed material systems of $A_3B_2C_9$ are experimentally feasible, because of the successful synthesis of $Cs_3In_2Cl_9$ and $Cs_3Fe_2Cl_9$ crystal. Our findings provide a platform for realizing high temperature QAHE in the intrinsic two-dimensional halide perovskite.

APPENDIX A: LAYERED STRUCTURE AND DISTORTED OCTAHEDRA STRUCTURE IN MONOLAYER $A_3B_2C_9$

As shown in Fig. 5, monolayer $A_3B_2C_9$ (A = Rb, Cs; B = Pd, Pt; C = Cl, Br) comprise the five atomic layers where the transitional metal atoms are embedded in the second and fourth layer. The octahedra around transitional metal atoms is distorted at some extent. Taking $Cs_3Pt_2Cl_9$ as an example, one can find the internal and external bond length between transition metal atom and halogen atom are different. Usually, d orbitals are split into t_{2g} and e_g groups in an octahedra crystal
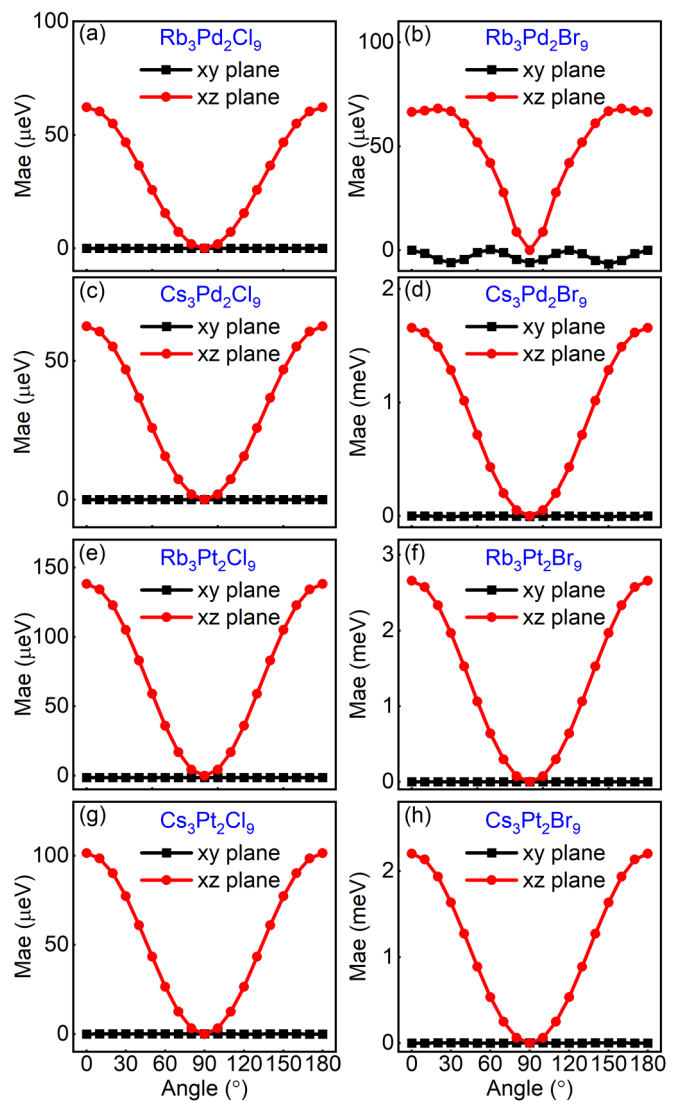

FIG. 7. (a)–(h) Magnetic anisotropy energy (MAE) of monolayers (a) $Rb_3Pd_2Cl_9$, (b) $Rb_3Pd_2Br_9$, (c) $Cs_3Pd_2Cl_9$, (d) $Cs_3Pd_2Br_9$, (e) $Rb_3Pt_2Cl_9$, (f) $Rb_3Pt_2Br_9$, (g) $Cs_3Pt_2Cl_9$, and (h) $Cs_3Pt_2Br_9$. There is an extremely small MAE (6.41 μeV) of $Rb_3Pd_2Br_9$ in the x-y plane.
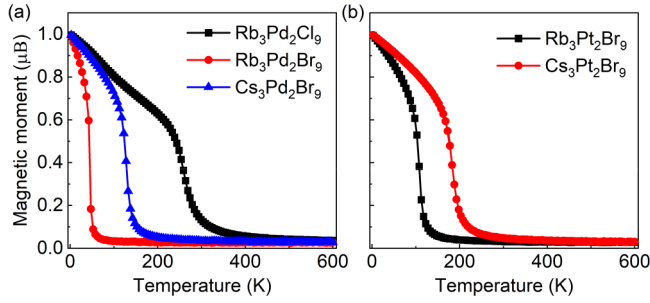
FIG. 8. (a),(b) Normalized magnetic moment of monolayers (a) $Rb_3Pd_2Cl_9$, $Rb_3Pd_2Br_9$, and $Cs_3Pd_2Br_9$ and (b) $Rb_3Pt_2Br_9$ and $Cs_3Pt_2Br_9$ as a function of temperature by Monte Carlo simulations.

field. In monolayer $A_3B_2C_9$, the distorted octahedra crystal field will further split t_{2g} group into a_g and e'_g required by D_3^2 space group, as shown in Fig. 5(c).

APPENDIX B: PHONON SPECTRUM OF MONOLAYER $A_3B_2C_9$

In Fig. 6, we plot the phonon spectrum of all monolayer $A_3B_2C_9$. The absence of imaginary frequency mode in monolayer $A_3B_2C_9$ indicates the stability of structures.

APPENDIX C: MAGNETIC PROPERTIES OF MONOLAYER $A_3B_2C_9$

In this part, we summarize the magnetic properties of monolayer $A_3B_2C_9$. Table II displays the total energy of all monolayer $A_3B_2C_9$ in the four magnetic configurations where the ferromagnetic and three kinds of antiferromagnetic states are considered. One can find that the ferromagnetic configuration is the ground state for all monolayer $A_3B_2C_9$.

Figure 7 displays the magnetic anisotropy energy (MAE) of monolayer $A_3B_2C_9$ (A = Rb, Cs; B = Pd, Pt; C = Cl, Br). The lower MAE within the x-y plane indicates that the magnetization direction prefers to lie in the x-y plane. Especially,

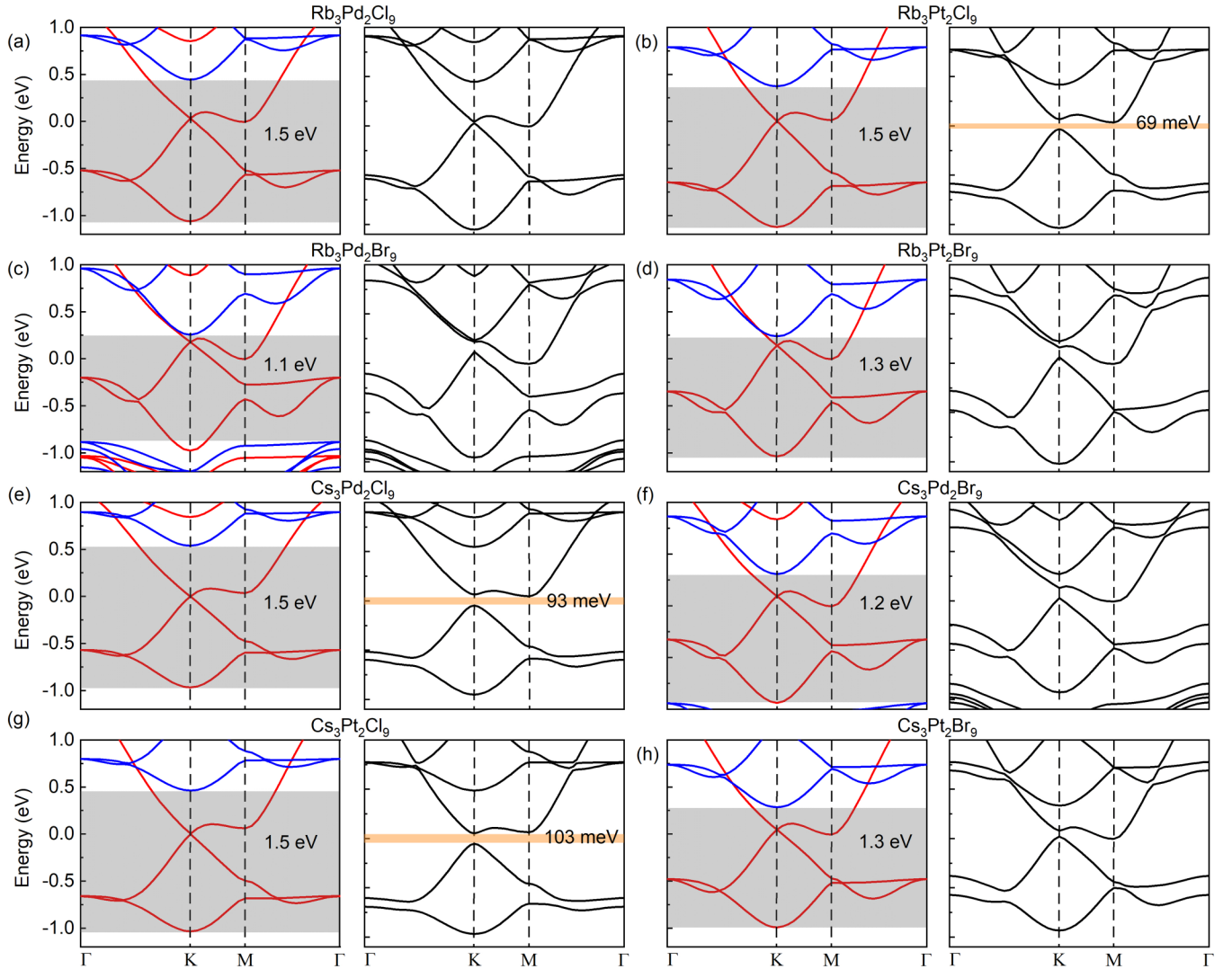FIG. 9. (a)–(h) Band structure of (a) $Rb_3Pd_2Cl_9$, (b) $Rb_3Pt_2Cl_9$, (c) $Rb_3Pd_2Br_9$, (d) $Rb_3Pt_2Br_9$, (e) $Cs_3Pd_2Cl_9$, (f) $Cs_3Pd_2Br_9$, (g) $Cs_3Pt_2Cl_9$, and (h) $Cs_3Pt_2Br_9$ without and with spin-orbit coupling.
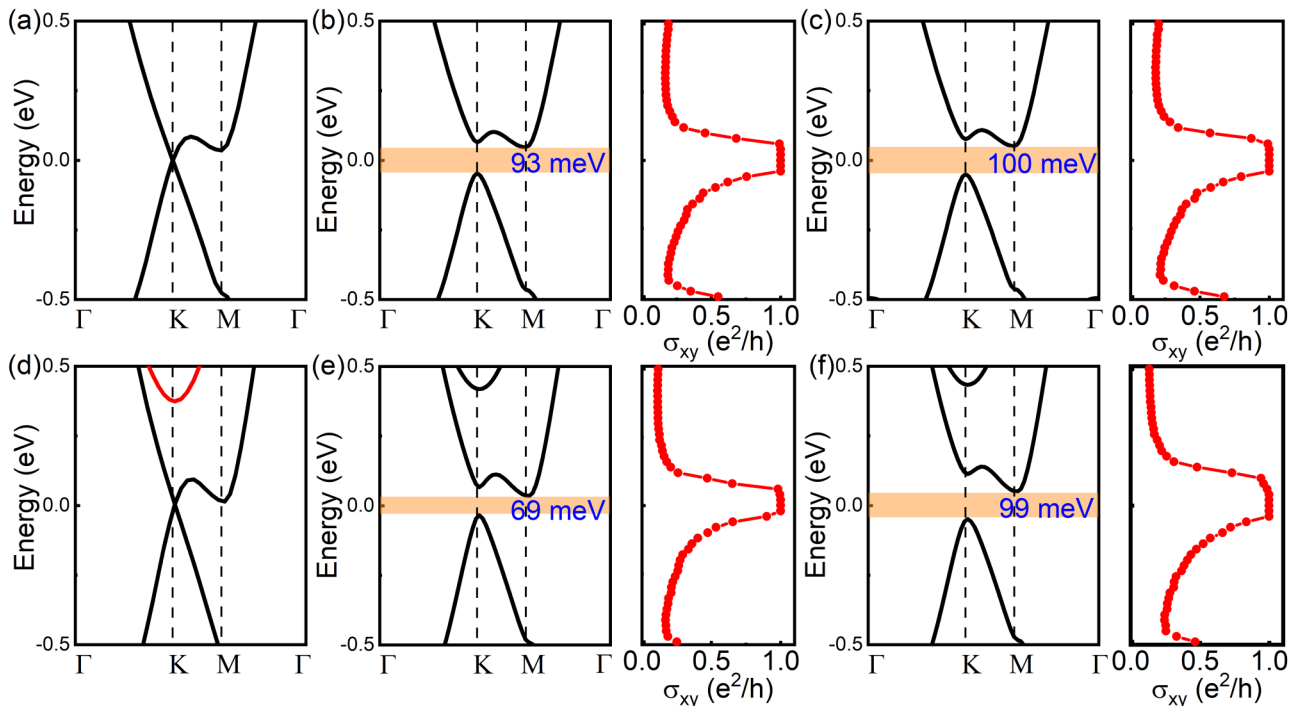
FIG. 10. (a)–(c) Band structure of $Rb_3Pt_2Cl_9$ without spin-orbit coupling. The band structure and anomalous Hall conductivity of $Rb_3Pt_2Cl_9$ with spin-orbit coupling when magnetization is along $\phi = 45°$. The band structure and anomalous Hall conductivity of $Rb_3Pt_2Cl_9$ with spin-orbit coupling when magnetization is along z direction; (d)–(f) the band structure of $Cs_3Pd_2Cl_9$ without spin-orbit coupling. The band structure and anomalous Hall conductivity of $Cs_3Pd_2Cl_9$ with spin-orbit coupling when magnetization is along $\phi = 45°$. The band structure and anomalous Hall conductivity of $Cs_3Pd_2Cl_9$ with spin-orbit coupling when magnetization is along z direction.

there is a tiny in-plane anisotropy(6 μeV) with a period of 60° in monolayer $Rb_3Pd_2Br_9$.

In Fig. 8, we plot the normalized magnetic moment of monolayers $Rb_3Pd_2Cl_9$, $Rb_3Pd_2Br_9$, $Cs_3Pd_2Br_9$, $Rb_3Pt_2Br_9$, and $Cs_3Pt_2Br_9$ as a function of temperature by Monte Carlo simulations. The critical temperatures of the Berezinskii-Kosterlitz-Thouless transition for monolayers $Rb_3Pd_2Cl_9$, $Rb_3Pd_2Br_9$, and $Cs_3Pd_2Br_9$ are 263, 47, and 127 K, respectively. For monolayers $Rb_3Pt_2Br_9$ and $Cs_3Pt_2Br_9$, the critical temperatures are 107 and 188 K, respectively.

APPENDIX D: BAND STRUCTURE OF MONOLAYER $A_3B_2C_9$ WITHOUT AND WITH SPIN-ORBIT COUPLING

As shown in Fig. 9, the band structures of all monolayer $A_3B_2C_9$ are depicted. In the absence of spin-orbit coupling, we can see that all $A_3B_2C_9$ monolayers are half metals with a Dirac point located at K point. The big energy windows with one spin channel (the gray area) range from 1.1 to 1.5 eV

exhibiting great promise for the application of spintronic devices. After taking spin-orbit coupling into consideration, the nontrivial global gaps can be opened in monolayers $Cs_3Pd_2Cl_9$, $Cs_3Pt_2Cl_9$, and $Rb_3Pt_2Cl_9$ with Chern numbers of $\mathcal{C} = \pm 1$ when the vertical mirror symmetry is broken.

APPENDIX E: TOPOLOGICAL PROPERTIES OF MONOLAYERS $RB_3Pt_2Cl_9$ AND $Cs_3Pd_2Cl_9$

In Fig. 10, we plot the band structures and anomalous Hall conductivity of monolayers $Rb_3Pt_2Cl_9$ and $Cs_3Pd_2Cl_9$, respectively. After the spin-orbit coupling is switched on a global band gap of 69 meV opens in $Rb_3Pt_2Cl_9$ with in-plane magnetization. And the gap can be further increased to 99 meV with out-of-plane magnetization. Similarly, in monolayer $Cs_3Pd_2Cl_9$, the global band gap increases from 93 meV to 100 meV when the magnetization direction is tuned from in plane to out of plane. The topological properties can be examined by the quantized anomalous Hall conductivity as shown in Figs. 10(b) and 10(c) and Figs. 10(e) and 10(f).

[1] K. V. Klitzing, G. Dorda, and M. Pepper, Phys. Rev. Lett. **45**, 494 (1980).

[2] F. D. M. Haldane, Phys. Rev. Lett. **61**, 2015 (1988).

[3] Z. Qiao, S. A. Yang, W.-X. Feng, W.-K. Tse, J. Ding, Y. G. Yao, J. Wang, and Q. Niu, Phys. Rev. B **82**, 161414(R) (2010).

[4] Z. Qiao, W. Ren, H. Chen, L. Bellaiche, Z. Zhang, A. H. MacDonald, and Q. Niu, Phys. Rev. Lett. **112**, 116404 (2014).

[5] R. Yu, W. Zhang, H. J. Zhang, S. C. Zhang, X. Dai, and Z. Fang, Science **329**, 61 (2010).

[6] S. Qi, Z. Qiao, X. Deng, E. D. Cubuk, H. Chen, W. Zhu, E. Kaxiras, S. B. Zhang, X. Xu, and Z. Zhang, Phys. Rev. Lett. **117**, 056804 (2016).

[7] P. Zhong, Y. Ren, Y. Han, L. Zhang, and Z. Qiao, Phys. Rev. B **96**, 241103(R) (2017).

[8] S. Qi, R. Gao, M. Chang, Y. Han, and Z. Qiao, Phys. Rev. B **101**, 014423 (2020).

[9] Z. Wang, C. Tang, R. Sachs, Y. Barlas, and J. Shi, Phys. Rev. Lett. **114**, 016603 (2015).

[10] C. Tang, B. Cheng, M. Aldosary, Z. Wang, Z. Jiang, K. Watanabe, T. Taniguchi, M. Bockrath, and J. Shi, APL Mater. **6**, 026401 (2018).

[11] C.-Z. Chang, J. S. Zhang, X. Feng, J. Shen, Z. C. Zhang, M. Guo, K. Li, Y. Ou, P. Wei, L.-L. Wang, Z.-Q. Ji, Y. Feng, S. H. Ji, X. Chen, J. F. Jia, X. Dai, Z. Fang, S.-C. Zhang, K. He, Y. Y. Wang *et al.*, Science **340**, 167 (2013).

[12] J. Li, Y. Li, S. Du, Z. Wang, B.-L. Gu, S.-C. Zhang, K. He, W. Duan, and Y. Xu, Sci. Adv. **5**, eaaw5685 (2019).

[13] M. M. Otrokov, I. P. Rusinov, M. Blanco-Rey, M. Hoffmann, A. Y. Vyazovskaya, S. V. Eremeev, A. Ernst, P. M. Echenique, A. Arnau, and E. V. Chulkov, Phys. Rev. Lett. **122**, 107202 (2019).

[14] Y. Deng, Y. Yu, M. Z. Shi, J. Wang, X. H. Chen, and Y. Zhang, Science **367**, 895 (2020).

[15] Y. Han, S. Sun, S. Qi, X. Xu, and Z. Qiao, Phys. Rev. B **103**, 245403 (2021).

[16] A. S. Bhalla, R. Guo, and R. Roy, Mater. Res. Innovations **4**, 3 (2000).

[17] J. B. Goodenough, Rep. Prog. Phys. **67**, 1915 (2004).

[18] M. A. Peña and J. L. G. Fierro, Chem. Rev. **101**, 1981 (2001).

[19] S. J. Kim, S. Lemaux, G. Demazeau, J. Y. Kim, and J. H. Choy, J. Mater. Chem. **12**, 995 (2002).

[20] G. Koster, L. Klein, W. Siemons, G. Rijnders, J. S. Dodge, C.-B. Eom, D. H. A. Blank, and M. R. Beasley, Rev. Mod. Phys. **84**, 253 (2012).

[21] H. Jin, J. Im, and A. J. Freeman, Phys. Rev. B **86**, 121102(R) (2012).

[22] C. Weeks and M. Franz, Phys. Rev. B **82**, 085310 (2010).

[23] R. Yu, H. Weng, Z. Fang, X. Dai, and X. Hu, Phys. Rev. Lett. **115**, 036807 (2015).

[24] Y. Chen, Y.-M. Lu, and H.-Y. Kee, Nat. Commun. **6**, 6593 (2015).

[25] D. Xiao, W. Zhu, Y. Ran, N. Nagaosa, and S. Okamoto, Nat. Commun. **2**, 596 (2011).

[26] A. M. Cook and A. Paramekanti, Phys. Rev. Lett. **113**, 077203 (2014).

[27] A. Rüegg, C. Mitra, A. A. Demkov, and G. A. Fiete, Phys. Rev. B **85**, 245131 (2012).

[28] H. S. Lu and G. Y. Guo, Phys. Rev. B **99**, 104405 (2019).

[29] T. L. Hodgkins, C. N. Savory, K. K. Bass, B. L. Seckman, D. O. Scanlon, P. I. Djurovich, M. E. Thompson, and B. C. Melot, Chem. Commun. **55**, 3164 (2019).

[30] W.-H. Guo, J.-J. Shi, Y.-H. Zhu, M. Wu, J. Du, Y.-L. Cen, S.-M. Liu, and S.-P. Han, Phys. Rev. Appl. **13**, 024031 (2020).

[31] J.-Y. You, Z. Zhang, B. Gu, and G. Su, Phys. Rev. Appl. **12**, 024063 (2019).

[32] X.-L. Sheng and B. K. Nikolić, Phys. Rev. B **95**, 201402(R) (2017).

[33] Q. Sui, J. Zhang, S. Jin, Y. Xia, and G. Li, Chin. Phys. Lett. **37**, 097301 (2020).

[34] Q. Liu, L. Wang, Y. Fu, X. Zhang, L. Huang, H. Su, J. Lin, X. Chen, D. Yu, X. Cui, J. W. Mei, and J. F. Dai, Phys. Rev. B **103**, 235411 (2021).

[35] H. Yamatera and K. Nakatsu, Bull. Chem. Soc. Jpn. **27**, 244 (1954).

[36] G. Kresse and J. Furthmüller, Phys. Rev. B **54**, 11169 (1996).

[37] J. P. Perdew, K. Burke, and M. Ernzerhof, Phys. Rev. Lett. **77**, 3865 (1996).

[38] H. J. Monkhorst and J. D. Pack, Phys. Rev. B **13**, 5188 (1976).

[39] A. Togo and I. Tanaka, Scr. Mater. **108**, 1 (2015).

[40] J. Paier, M. Marsman, K. Hummer, G. Kresse, I. C. Gerber, and J. G. Ángyán, J. Chem. Phys. **124**, 154709 (2006).

[41] A. A. Mostofi, J. R. Yates, Y.-S. Lee, I. Souza, D. Vanderbilt, and N. Marzari, Comput. Phys. Commun. **178**, 685 (2008).

[42] X. Wang, J. R. Yates, I. Souza, and D. Vanderbilt, Phys. Rev. B **74**, 195118 (2006).

[43] Q. S. Wu, S. N. Zhang, H.-F. Song, M. Troyer, and A. A. Soluyanov, Comput. Phys. Commun. **224**, 405 (2018).

[44] L. Liu, X. Ren, J. Xie, B. Cheng, W. Liu, T. An, H. Qin, and J. Hu, Appl. Surf. Sci. **480**, 300 (2019).

[45] S. Yang, L. Wang, S. Zhao, A. Liu, Y. Zhou, Q. Han, F. Yu, L. Gao, C. Zhang, and T. Ma, Appl. Mater. Interfaces **12**, 44700 (2020).

[46] L. Wang, T. Maxisch, and G. Ceder, Phys. Rev. B **73**, 195107 (2006).

[47] N. D. Mermin and H. Wagner, Phys. Rev. Lett. **17**, 1133 (1966).

[48] H. L. Zhuang and R. G. Hennig, Phys. Rev. B **93**, 054429 (2016).

[49] M. Ashton, D. Gluhovic, S. B. Sinnott, J. Guo, D. A. Stewart, and R. G. Hennig, Nano Lett. **17**, 5251 (2017).

[50] X. Liu, H.-C. Hsu, and C.-X. Liu, Phys. Rev. Lett. **111**, 086802 (2013).

[51] Y. Ren, J. Zeng, X. Deng, F. Yang, H. Pan, and Z. Qiao, Phys. Rev. B **94**, 085411 (2016).

[52] Z. Liu, G. Zhao, B. Liu, Z. F. Wang, J. Yang, and F. Liu, Phys. Rev. Lett. **121**, 246401 (2018).

[53] C. Gong, L. Li, Z. Li, H. Ji, A. Stern, Y. Xia, T. Cao, W. Bao, C. Wang, Y. Wang, Z. Q. Qiu, R. J. Cava, S. G. Louie, J. Xia, and X. Zhang, Nature (London) **546**, 265 (2017).